Original scientific paper

INTERLAYER EFFECT ON DEFORMATION AND FRACTURE OF DENDRITIC STRUCTURE FORMED DURING WIRE-FEED ELECTRON-BEAM ADDITIVE MANUFACTURING OF AL-SI ALLOY

Ruslan Balokhonov[1], Veronika Utyaganova[1], Diana Gatiyatullina[1,2], Aleksandr Zemlianov[1], Varvara Romanova[1]

[1]Institute of Strength Physics and Materials Science SB RAS, Russia
[2]National Research Tomsk State University, Russia

Abstract. *Interfaces and surfaces play an important role in tribology, mechanics and materials science, causing plastic strain localization and stress concentration of different spatial scales. The interfacial inhomogeneity is highly pronounced in 3D printed materials due to thermo-cycling and layer-by-layer building. In this paper, the inlayer and interlayer structure of a eutectic Al-Si alloy fabricated by wire-feed electron-beam additive manufacturing is investigated by optical and electron microscopy. Model structures inheriting the experimental morphology are created, and their deformation and fracture are simulated using ABACUS/Explicit, with the user-defined subroutines being developed to describe the constitutive behavior of aluminum dendrite, silicon and eutectic materials. A two-scale computational approach is implemented to study the influence of the interlayer formed in the heat-affected zone on the dendritic structure strength.*

Key words: *Additive manufacturing, Aluminum alloys, Microstructure, Multiscale numerical simulation, Plastic deformation, Fracture*

1. INTRODUCTION

Tribology is a multidisciplinary science that requires considering solid as a multiscale system, where deformation and fracture develop at different time and scale levels [1]. For instance, the macroscopic contact mechanics has to consider, at least phenomenologically, the atomic-scale interactions, the adhesion, the influence of plasticity and internal stresses, etc. [2]. In the interplay of tribology, mechanics and materials science, the key role belongs

to rough surfaces and curvilinear interfaces between the microstructural components: matrix and particles, coating and substrate, polycrystalline grains, layers, interlayers, etc. The interfacial and surface asperities are the sources of stress concentration and plastic strain localization of different spatial scales, which may result in earlier crack nucleation and growth causing premature material failure [1, 3]. The multiscale nature of deformation is most pronounced in additively manufactured materials with distinct interfaces formed due to the layer-by-layer fabrication of the sample and the material thermo-cycling in between the layers during melting.

Additive manufacturing has been ever increasingly used in a variety of industries due to its capacity of fabricating products of intricate shapes with an optimal consumption of materials [4, 5]. An application of additive technologies allows reducing the weight and accelerating the fabrication of components critical for the production process [4, 6], as well as minimizing the material and energy consumption via a recovery of used rebuildable components [7]. The aluminum alloys used in additive manufacturing are attractive materials due to their high specific strengths and cost-effective recycling [8]. The aluminum-silicon alloys possess low thermal expansion coefficients and high corrosion- and wear resistance [9, 10]. An addition of Si also improves the characteristics of casting and mechanical treatment of these alloys [11]. The material microstructure depends on the technological process parameters, especially on the alloy solidification rate [12, 13]. On the whole, the eutectics is a strengthening phase, but its coarse-grained and agglomerated structures may decrease the product strength and plasticity [14, 15]. Among the most popular printing processes are the laser- and electron-beam melting [16, 17]. The selective laser melting (SLM) of eutectic silumines selectively melts the powder by a laser beam along the scanning trajectory [18]. The wire-feed technologies have acquired an ever increasing application; they are efficient in printing of industrial prototypes and assembly components. The use of wires as the initial stock in laser melting processes allows saving more energy than in SLM [19]. The processing conditions necessary for a stable deposition of an Al 5087 wire were studied by a laser beam forming single- and multiple-layer strips [20]. The electron beam wire-feed additive manufacturing (EBAM) has clear advantages over the laser beam process, since it occurs in vacuum, which rules out an oxidation of aluminum alloys, and the energy density and the depth of thermal energy penetration are much higher than those of a laser [21, 22].

The additively manufactured alloys differ from the conventional cast alloys of the same chemical compositions by their complex hierarchical structure with characteristic features at different scale levels [23]. Earlier we demonstrated that the material inside individual layers of EBAM Al-Si12 alloy represent a two-level composite [24]. On a scale of tens of microns there are aluminum dendrites surrounded by a eutectic network that at a lower level represents an aluminum matrix with volumetric silicon particles measuring hundreds of nanometers [25].

The purpose of this work is to study experimentally the EBAM Al-Si12 alloy material structure in the heat affected zone between the layers and the common features of deformation and fracture of composites at different scale levels using the methods of numerical modeling.

2. Wire-Feed Additive Manufacturing of Al-Si12 Alloy and Microstructure Analysis

Using an *ad hoc* setup designed and built at the Institute of Strength Physics and Materials Science SB RAS (Tomsk, Russia), we fabricated a bulk sample shaped as a thin-walled product (Fig. 1a). The material used for printing was a 1.2 mm wire of a eutectic alloy, AlSi12 ESAB OK Autrod 4047, which was deposited on a 5 mm-thick substrate of an AlMg5 alloy. The chemical compositions of both alloys (AlSi12 and AlMg5) are listed in Table 1. The manufacturing followed an optimal regime of an exponential decrease of the heat input, which allows fabricating the samples with a minimal content of defects, such as porosity and discontinuities, and prevents the spread of the top layers. The heat input was calculated by the following formula: $HI = (U \cdot I \cdot 60)/(V \cdot 1000)$, where U – accelerating voltage (V), I – current (A), V – table motion velocity (mm/min). In this case, the heat input values were changed due to the exponentially decreasing current on every layer during printing of the sample. The heat input dependence of a layer-by-layer printing of AlSi12 alloy is given in Fig. 1b.
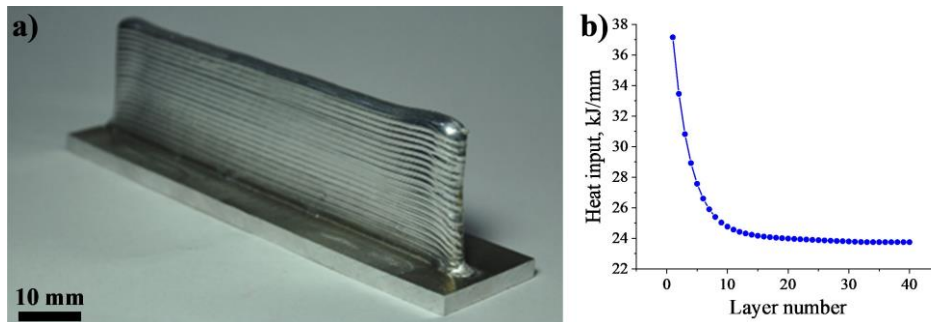
Fig. 1 Thin-walled AlSi12 alloy sample fabricated by wire-feed EBAM (a) heat input parameters during layer-by-layer printing (b)

Table 1 Compositions of AlMg5 Substrate and AlSi12 Wire

| Alloy	Al, %	Mg, %	Si, %	Mn, %	Fe, %	Cr, %	Ti, %	Zn, %	V, %	Zr, %
AlMg5	Balance	5.21	0.41	0.48	0.43	0.23	0.11	0.16	-	-
AlSi12	Balance	-	13.3	-	0.11	0.08	0.03	-	0.035	0.005

The EBAM sample structure was examined by metallography and scanning and transmission electron microscopy (SEM, TEM). The metallographic tests were performed using a standard technique. The samples with a size of 10x10 mm were cut from the middle part of the EBAM workpiece, ground on an abrasive paper with a grit of 200 to 2000, and polished on diamond paste and suspension. The surfaces of metallographic sections were examined in an Olympus LEXT OLS4100 laser scanning confocal microscope. The sample microstructure was studied in the TESCAN VEGA II LMU and LEO EVO-50 scanning electron microscopes (SEM); the latter was equipped with a system for the energy dispersive microanalysis (EDS). Thin foils for TEM examinations were prepared by thinning the samples cut from the thin-walled workpiece fragments to a thickness of ~ 160 μm via mechanical grinding on abrasive paper and using an EM-09100IS ion slicer at 7 kV

for 7–8 hrs. The fine structure was studied in a JEM-2100 transmission electron microscope (TEM, Tokyo Boeki Ltd., Japan) at an accelerating voltage of 200 kV.

The studies performed in this work have demonstrated that the AlSi12 EBAM alloy has a complex hierarchical microstructure at different scale levels with characteristic features of the layer-by-layer printing, which distinctly differs from a typical microstructure of the cast AlSi12 alloy in terms of its morphology and phase distribution (Fig. 2). Inside the printed layers, there are large dendrites in a network (Fig. 2a). In-between the layers, immediately in the electron beam affected zone, a 30–50 µm-thick interlayer is formed, containing large particles (Fig. 2b).
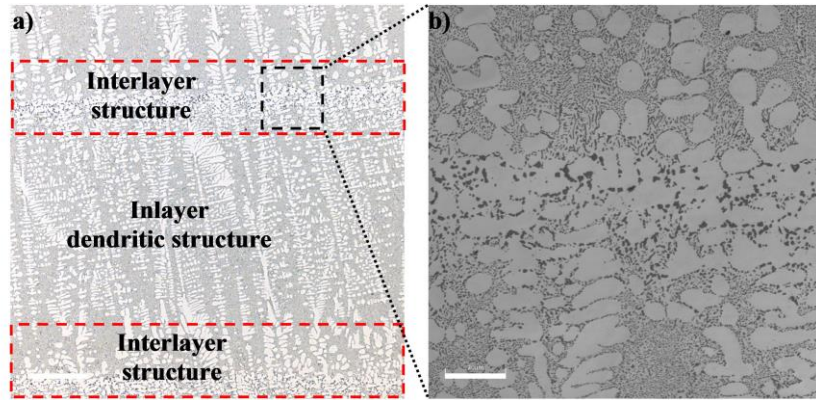

Fig. 2 Optical images of AlSi12 EBAM alloy at a scale of 100 (a) and 20 µm (b)
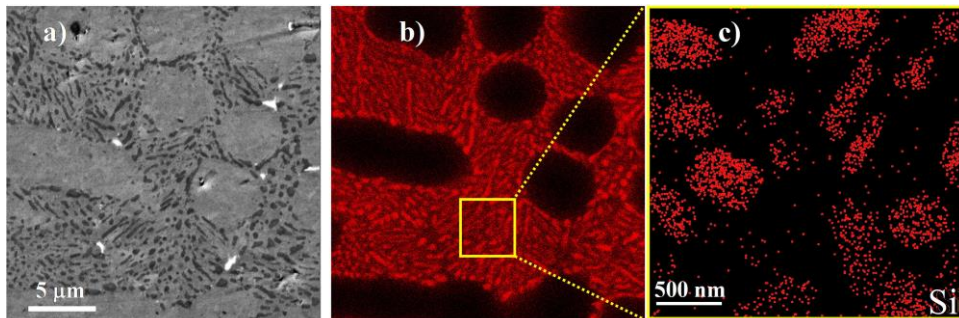
Fig. 3 SEM images inside AlSi12 layer: in SE beams (a) and EDS mapping of this area (b). TEM EDS mapping of fine eutectic structure (c)

The dendritic structure inside the layer represents a two-level composite material (Fig. 3a). At a scale of tens of microns (Level 1), it consists of plastic inclusions in the form of dendrites of a primary solid solution of α-aluminum in a harder matrix representing a eutectic network (Fig. 3b). At a lower micron scale (Level 2), the eutectics, in its turn, is revealed by TEM as volumetric submicron silicon particles in an aluminum matrix (Fig. 3c) and, therefore, represents a metal-matrix composite material. Silicon particles in the eutectics have a variety of shapes (rectangular, oval, rounded and elongated tooth-like

shapes). The particle size in the dendritic interlayer is several times larger than that of silicon particles in the eutectics (cf. Figs. 4c and 3c). To sum up, the interlayer material, similarly to the eutectic material, is a composite with micron particles forming a cellular substructure rather than a structure with uniformly distributed silicon submicron-sized particles. It was also shown in the works of some authors studying the microstructure of AM materials, manufactured by SLM (e.g. [22]), that the structure morphology in the heat affected zone (HAZ) in eutectic aluminum-silicon alloys differs from that inside the layer. They [22] attribute the precipitation of coarse silicon particles to high temperature gradients in the HAZ.
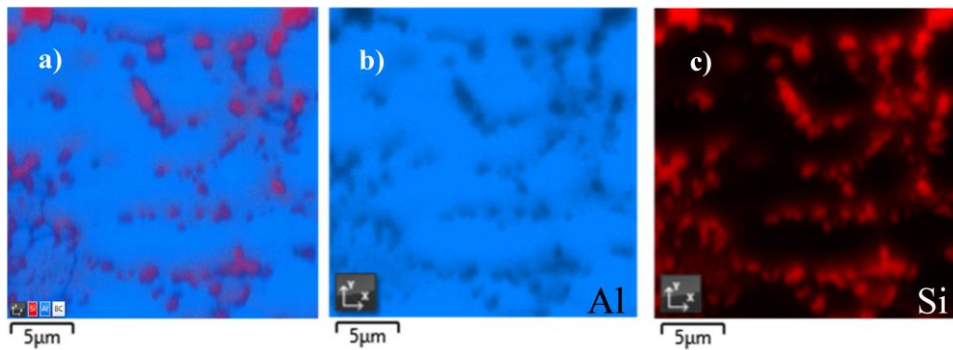

Fig. 4 SEM EDS mapping of an area in AlSi12 alloy in-between layers (a) and aluminum (b) and silicon (c) distribution patterns

3. COMPUTATIONAL ANALYSIS OF DEFORMATION AND FRACTURE IN DENDRITIC STRUCTURES

Using the experimental data presented in Figs. 2b and 3c, we designed the model structures at Level 1 (Fig. 5a and b) and the structures of an *aluminum matrix – silicon particle* composite at Level 2 (Fig. 5c). An explicit three-phase model structure (Fig. 5a), which is formed in-between the layers in the HAZ, contains an interlayer of large silicon particles. A two-phase *dendrites–eutectics* model structure (Fig. 5b), typical for the in-layer material, was designed relying on two considerations necessary for a *caeteris paribus* comparative analysis. Firstly, the dendrite morphology both in the interlayer area and outside it has to be consistent with that in the three-phase structure. Secondly, the total volume fraction of aluminum in the dendrites and the eutectic network has to be the same for the two- and three-phase structures and be equal to 86% (typical for AlSi12). Henceforward the term "phase" has no conventional physical meaning and is used only to distinguish between "dendrites-eutectic" and "dendrites-eutectic-interlayer" structures.

The dendritic structures (Fig. 5a, b) are of the sizes on the order of 100x100 µm and are discretized by a regular grid containing 1000×1000 square finite elements. The 2.5x2.5 µm model of the eutectic material (Fig. 5c) is approximated by a 480x480 mesh. The dynamic boundary-value problems on loading the composites are solved in a three-dimensional formulation simulating a plane strain state using ABAQUS/Explicit in a two-level approach. Firstly, at Level 2 we solve the problem of an elastic-plastic deformation of a

metal-matrix composite and then by averaging over the volume we identify the effective properties of the eutectic material. Then these properties are used at Level 1 in the numerical study of the plastic strain localization and crack propagation in the dendritic structures under tension.

Level 1 **Level 2**
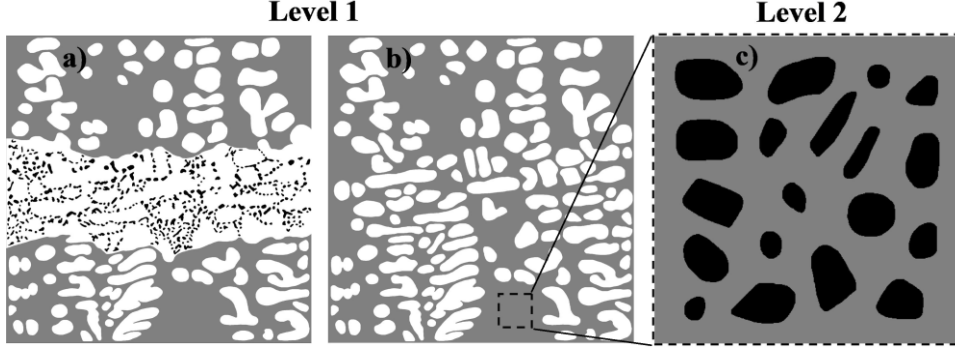
Fig. 5 Model structures: dendritic structures in HAZ (a) and inside the layer (b) and composite material in the eutectic network (c)

In order to describe the elastic-plastic behavior of aluminum, we used the Hooke's law:

$$\dot{\sigma}_{ij} = -\dot{P}\delta_{ij} + \dot{S}_{ij} = K\dot{\varepsilon}_{kk}\delta_{ij} + 2\mu(\dot{\varepsilon}_{ij} - \dot{\varepsilon}_{kk}\delta_{ij}/3 - \dot{\varepsilon}^{p}_{ij}),$$ (1)

where σ_{ij} and S_{ij} are the stress tensor and deviatoric tensor component, P is the pressure, ε_{ij} and $\varepsilon^{p}{}_{ij}$ are the total and plastic deformation components, δ_{ij} is the Kronecker delta, K and μ are the bulk and shear moduli; the upper dot indicate the time derivatives.

The plastic strain rate is found according to the associated plastic flow rule. The yielding condition includes the isotropic strain hardening into consideration:

$$F(\varepsilon^{p}) = \sigma_{u} - (\sigma_{u} - \sigma_{y})\exp(-\varepsilon^{p}/\varepsilon^{p}_{r}),$$ (2)

where σ_{u} and σ_{y} are the ultimate stress and the yield point, respectively, and $\varepsilon^{p}{}_{r}$ characterizes the strain hardening degree.

Silicon particle in the eutectic network and in the interlayer are assumed to be elastic and do not fracture. Cracks nucleate both in the aluminum and in the eutectics as soon as the accumulated equivalent plastic strain reaches its respective critical value:

$$\varepsilon^{p} = \varepsilon^{p}_{cAl} \text{ or } \varepsilon^{p} = \varepsilon^{p}_{cEut}.$$ (3)

Taking into account the models given by (1–3), a VUMAT user subroutine was developed for ABAQUS/Explicit, which was used to simulate a kinematic tension of the structures.

The elastic moduli of aluminum and silicon were taken from a reference book. The plasticity characteristics in the dendrites and the eutectics were assumed to be different; they were selected based on the concept of a dislocation mean free path to their pinning sites, which is determined either by the average size of dendrites (about 5–10 µm) or the average spacing between the silicon particles in the eutectic network (about 0.5–1 µm). In

a manner similar to the Hall–Petch law, the yield stress and plasticity of aluminum in the dendrites or eutectics were selected in accordance with the experimentally obtained flow curves for the aluminum samples with the corresponding grain sizes [26, 27].

The elastic modulus values for the eutectic material in the dendritic structures at Level 1 (Fig. 5a, b) were calculated based on the aluminum volume fraction in the composite of $\varphi=74\%$ at Level 2 (Fig. 5c):

$$K^{Eut} = K^{Al}\varphi + K^{Si}\left(1-\varphi\right), \mu^{Eut} = \mu^{Al}\varphi + \mu^{Si}\left(1-\varphi\right). \tag{4}$$

The parameters of the hardening function (2) for the eutectic material at Level 1 were obtained by calculating the composite tension at Level 2 via averaging of the equivalent stresses $\langle\sigma\rangle$ and accumulated equivalent plastic strains $\langle\varepsilon^p\rangle$ over the domain shown in Fig.5c, followed by an approximation of the resulting relationship

$$F^{Eut}\left(\varepsilon^p\right) = \langle\sigma\rangle\left(\langle\varepsilon^p\rangle\right) = \sigma_u^{Eut} - \left(\sigma_u^{Eut} - \sigma_y^{Eut}\right)\exp\left(-\varepsilon^p/\varepsilon_r^{pEut}\right). \tag{5}$$

The results of modeling the composite tension at Level 2 are given in Fig. 6. Due to a difference between the elastic moduli of aluminum and silicon, a stress concentration in the vicinity of the matrix–aluminum interface is observed as early as in the elastic deformation stage. Upon further loading, plastic shears develop in the matrix in the sites of the highest stress concentrations, which propagate throughout the composite volume in-between the particles and form plastic shear localization bands at an angle 45 degrees to the axis of tension (Fig. 6c). Within the stages of a developed plastic flow, the level of stresses in the particles is about 2–3 times higher than that in the matrix (cf. Fig. 6a and b).

The averaged flow curve of the eutectic composite is presented in Fig. 6d. By approximating this curve, we obtained the yield stress and strength values and those of the hardening coefficient in (5). These properties are used as the characteristics of plasticity and isotropic hardening of the eutectic network material during deformation of dendritic structures at Level 1. The values of the model constants are listed in Table 2.

The results of modeling the dendritic structure deformation are presented in Figs. 7–10. Figure 7 illustrates the stressed state in the developed plastic flow stage of the composites. The eutectic network withstands a more than twice higher stress level than do the aluminum dendrites (compare pairwise Fig. 7a, c and b, d). This is accounted for by two factors. Firstly, aluminum in the eutectic network, due to a nearly an order of magnitude smaller dislocation mean free path, demonstrates higher strength characteristics, corresponding to its submicrocrystalline state, than aluminum in the micron-sized dendrites. Secondly, the submicron silicon particles in the eutectic network cause an additional strengthening effect.
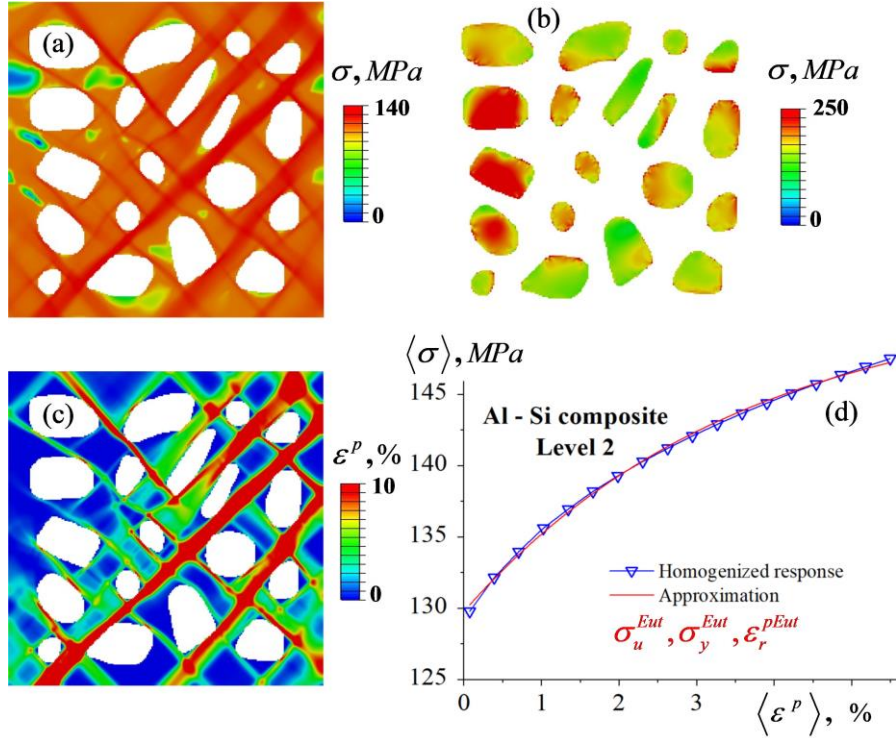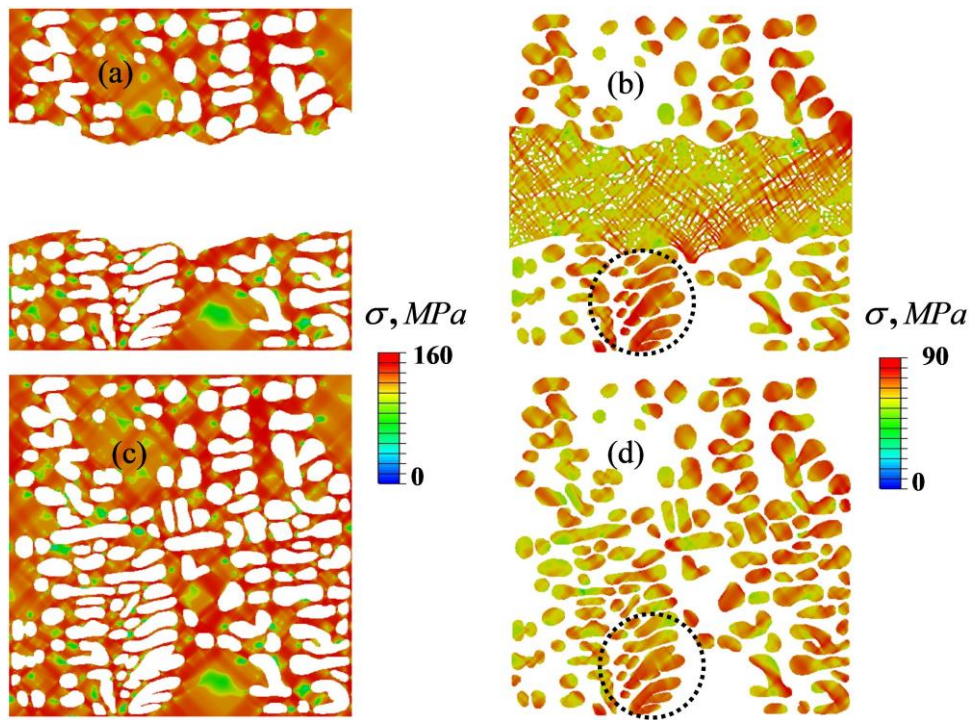
Fig. 6 Equivalent stress distribution in aluminum matrix (a) and silicon particles (b), accumulated equivalent plastic strain (c) at 3 % homogenized deformation of eutectic composite (d)

Table 2 Model parameters

| Material	ρ, g/cm³	$\mathbf{K}$, GPa	μ, GPa	σ_y, MPa	σ_u, MPa	ε_r^p, %	ε_c^p, %
Al in Eutectics	2.7	66	26	125	150	20	-
Al in Dendrites	2.7	66	26	60	100	20	90
Eutectics	2.6	74	36	130	157	5	50
Si	2.33	98	60	-	-	-	-

By performing a pairwise comparison of Fig. 7a, b and c, d, we can reveal the following interlayer effect. On the whole, the stressed state of the eutectics outside the interlayer area hardly depends on its presence (cf. Fig. 7a and c). The situation in the dendrites due to the presence of an interlayer is somewhat different. Owing to the availability of comparatively large silicon particles, a specific inhomogeneous stressed state pattern is formed: thin lengthy stress concentration regions are found in-between the particles, forming a characteristic net- structure (Fig. 7b). Because of the interlayer, there are quantitative differences in the regions delineated by dashed circles: the stress concentration in these regions is higher in the three-phase structure than it is in the two-phase structure (cf. Fig. 7b and d).

Fig. 7 Equivalent stress distributions in eutectic network (a, c) and aluminum dendrites in matrix (b, d) in pre-fracture stage of dendritic structures with (a, b) and without (c, d) interlayer taken into consideration

The fine net-structure of the stressed state in the interlayer with characteristic narrower stress concentration regions results from the plastic strain localization in-between the silicon particles (Fig. 8). High stress concentrations near the silicon particles/aluminum interface, which are generated as early as in the stage of elastic deformation of the three-phase dendritic structure, cause a nucleation of the local sites of plastic deformation in the region of interfacial asperities. As the loading increases, the entire interlayer is covered by a system of localized shear bands, with the regions of the highest localization being observed along the interface between the interlayer and the eutectic network (dashed squares in Fig. 8b). Such an intensive deformation of the interlayer in the three-phase structure results in a redistribution of the stress-strain state and a much stronger strain localization in some regions of the dendritic structure surrounding the interlayer compared to the two-phase structure case (compare pairwise the areas delineated by dashed circles in Fig. 8a, b and c, d).
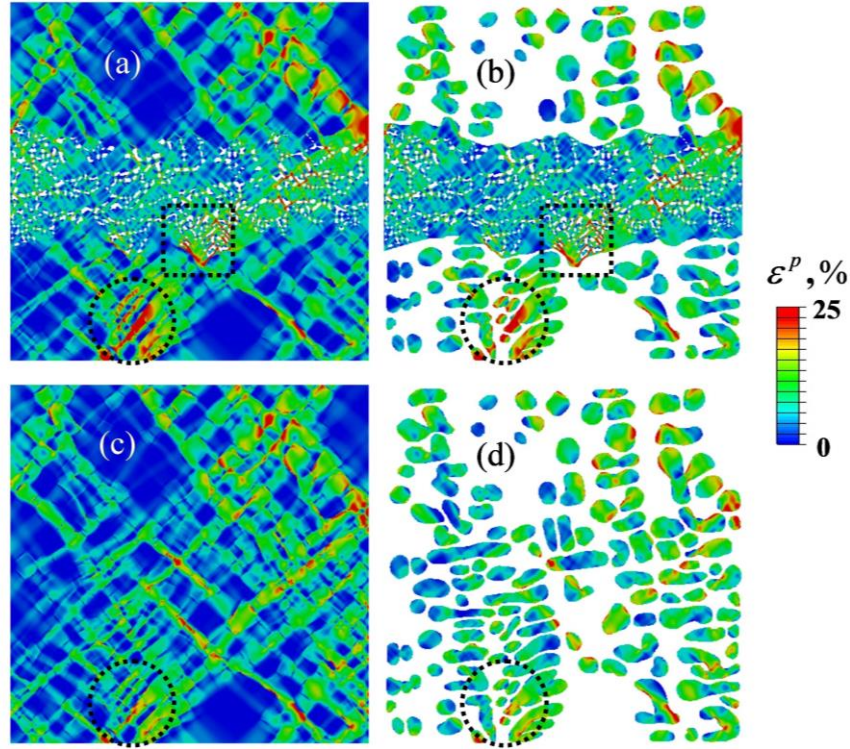
Fig. 8 Equivalent plastic strain distributions in the entire volume (a, c) and in separate aluminum dendrites (b, d) in pre-fracture stage of dendritic structures with interlayer (a, b) taken into consideration and without it (c, d)

Figure 9a presents the probability densities of plastic strain distribution over the volume in the two-phase and three-phase structures, calculated on the data of Figure 8, separately for the dendrites and the eutectic network. We have found out that the eutectic network has been deformed rather weakly: the major part of its volume experienced small plastic strains of fractions of a percent (peaks in the curves with square symbols in Fig. 9a). Note that the strain localization patterns are quantitatively identical for the two- and three-phase structures (blue and purple curves with square symbols in Fig. 9a coincide). The main differences are observed in the aluminum dendrites straining with a higher intensity than the eutectic network. A large volume fraction of dendrites, both in the three- and two-phase structures, experiences a strain of 5–8 % (major peaks in curves with triangular symbols in Fig. 9a). It is noteworthy that, similarly to the eutectic network, there are peaks at the plastic strain of parts of a percent, but their volume fraction is much smaller. In the three-phase structure, there are more regions with a plastic deformation of 8–20 % and a smaller number of those where the deformation is in the range of 1–5 %, than in the two-phase structure (Cf. blue and red curves with triangular symbols in Fig. 9a). The regions with pronounced plastic strain localization occupy equal volume fractions in the two- and three-phase structures: blue and red curves with triangular symbols in Fig. 9 coincide for deformations of more than 20%.
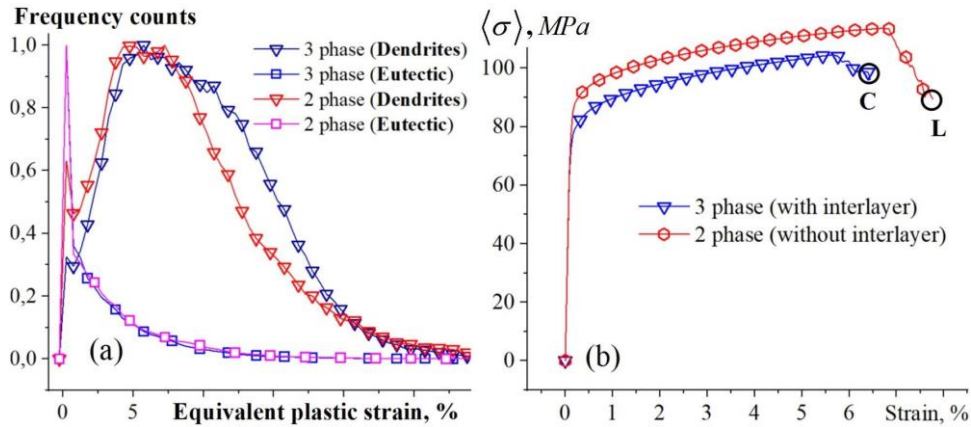
Fig. 9 Probability densities constructed for distributions in Fig. 8 (a) and flow curves of dendritic structures with and without interlayer taken into consideration (b). States C and L are shown in Fig. 10 c and l

The macroscopic response of the composite dendritic structures under tension is given in Fig. 9b, where *Strain* is the relative elongation of the computational domains. Two main conclusions can be made at this point. Firstly, the two-phase structure withstands a higher stress level than the three-phase structure. This occurs due to the following circumstance. Despite the fact that the aluminum and silicon volume fractions in the two- and three-phase structures are the same (86 % Al and 14% Si), the volume fraction of the eutectics is larger in the two-phase structure. Therefore, the latter contains a larger volume fraction of the high-strength aluminum, wherein the dislocation free mean path is an order of magnitude shorter than that in low-strength aluminum in the dendrites. Secondly, the strength of the two-phase structure without an interlayer is higher than that of the structure with an interlayer. This is related to the above-described character of plastic strain localization in the interlayer and its effect on the material stress-strain state beyond the interlayer. Thus, a higher stress concentration and plastic strain localization in the area of the interlayer–eutectic network interface causes an earlier crack nucleation (Fig. 10a) than this occurs in the two-phase structure (Fig. 10j).

The crack propagation character in both structures is similar. The first fractured regions appear in the aluminum dendrites. However, these fracture events are few; further on all secondary cracks nucleate in the eutectics in the vicinity of the interface with the dendrites in the cases where the equivalent plastic strain reaches its critical value ε_{cEut}^{p} (Fig. 10d, m). Primarily, these cracks propagate in the inter-dendritic space from one interface to another and stop (Fig. 10e, n). A high stress concentration in the crack tip results in an intensive plastic strain localization in the dendrites, which is accumulated up to its critical value ε_{cAl}^{p} and the cracks grow through the dendrites (Fig. 10 f-i and o-r).
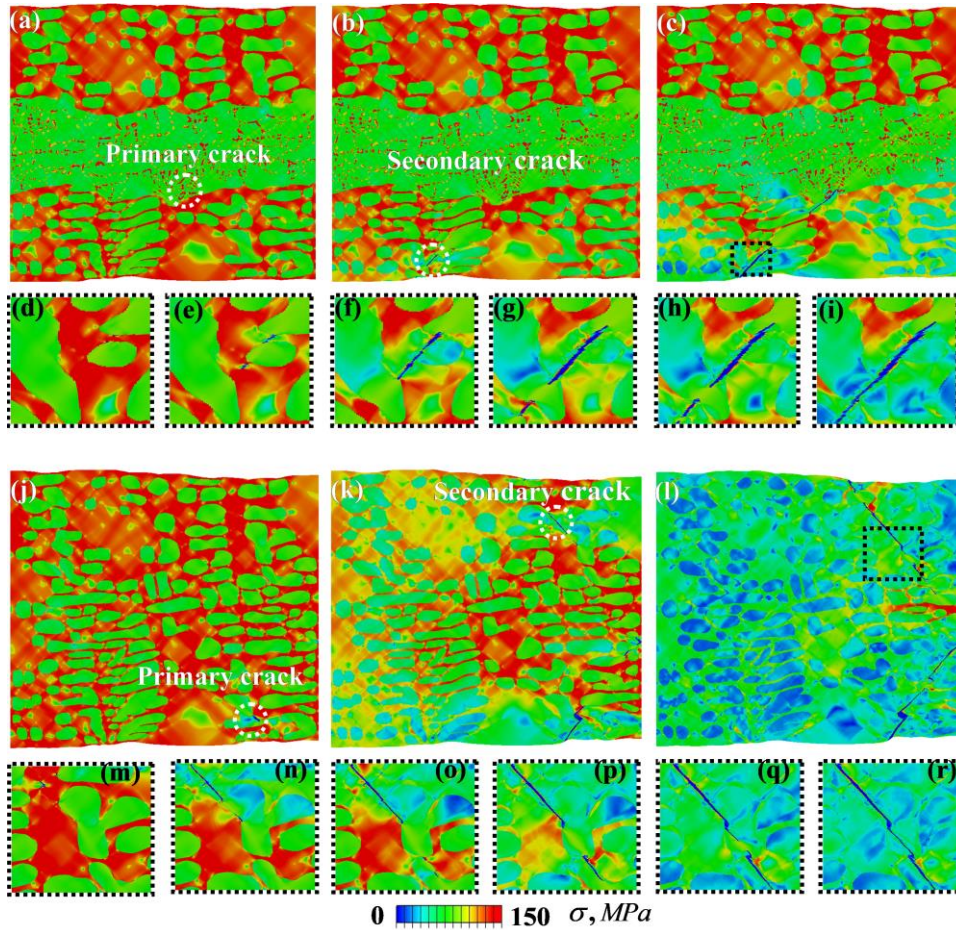
Fig. 10 Equivalent stress during fracture of dendritic structures with (a–i) and without (j–r) interlayer

4. CONCLUSIONS

Using the methods of optical and electron microscopy, we have experimentally studied the microstructure of an Al-Si12 eutectic alloy fabricated by the additive layer-by-layer electron-beam wire melting. The results demonstrated that inside every layer the aluminum dendrites measuring tens of microns are formed, which are surrounded by a eutectic network. The eutectic network is identified by transmission microscopy as an aluminum matrix with volumetric homogeneously distributed primary-silicon submicron-sized particles. It was found out that in-between the layers in the heat affected zone an interlayer is formed from aluminum inherited from the dendrites. The interlayer contains agglomerated micro-sized silicon particles that are distributed inhomogeneously in the form of a cellular structure. Based on the experimentally obtained images, a number of

model structures were designed: dendritic structures with and without interlayer and a composite eutectic material structure. In order to describe the mechanical response of silicon and aluminum, we used the isotropic constitutive models of elasticity and elasticity-plasticity including fracture, respectively. The structures and the models were integrated into ABAQUS/Explicit. The calculations of the composite structure tension were performed. A two-level approach was implemented, involving a primarily solution of the problem of a deformed *aluminum matrix – silicon particle*s composite at the micro level and, by averaging over the volume, the effective properties of the eutectic network were identified. These properties were then used at the level of hundreds of microns in order to study the deformation and fracture of the dendritic structures. The results of modeling demonstrate that in the interlayer in the region of its interface with the eutectic network a high stress concentration is formed, which results in a plastic flow localization, an early crack nucleation, and a decreased strength of the dendritic structure.

REFERENCES

1. Ostermeyer, G.-P., Popov, V.L., Shilko, E.V., Vasiljeva O.S., 2021, *Multiscale biomechanics and tribology of inorganic and organic systems*, STME Springer, Cham, 565 p.
2. Goryacheva, I.G., Paggi, M., Popov, V.L., 2021, *Editorial: Contact mechanics perspective of tribology*, Frontiers in Mechanical Engineering, 7, 649792.
3. Balokhonov, R., Romanova, V., Schwab, E., Zemlianov, A., Evtushenko, E., 2021, *Computational microstructure-based analysis of residual stress evolution in metal-matrix composite materials during thermomechanical loading*, Facta Universitatis-Series Mechanical Engineering, 19, pp. 241-252.
4. Zhao, N., Parthasarathy, M., Patil, S., Coates, D., Myers, K., Zhu, H., Li, W., 2023, *Direct additive manufacturing of metal parts for automotive applications*, Journal of Manufacturing Systems, 68, pp. 368-375.
5. Herzog, D., Seyda, V., Wycisk, E., Emmelmann, C., 2016, *Additive manufacturing of metals*, Acta Materialia, 117, pp. 371-392.
6. Kaur, I., Singh, P., 2021, *Critical evaluation of additively manufactured metal lattices for viability in advanced heat exchangers*, International Journal of Heat and Mass Transfer, 168, 120858.
7. Wasono, R.S., Wahab, D.A., Azman, A.H., 2019, *Additive manufacturing for repair and restoration in remanufacturing: An overview from object design and systems perspectives*, Processes, 7, 802.
8. Kiani, P., Dupuy, A. D., Ma, K., Schoenung, J. M., 2020, *Directed energy deposition of AlSi10Mg: Single track nonscalability and bulk properties*, Materials & Design, 194, 108847.
9. Zolotorevsky, V.S., Belov, N.A., Glazoff, M.V., 2007, *Casting aluminum alloys*, Elsevier Ltd., Amsterdam, 544 p.
10. Apelian, D., 2009, *Aluminum cast alloys: Enabling tools for improved performance*, North American Die Casting Association, Wheel Illinois, 60 p.
11. Ye, H., 2003, *An overview of the development of Al-Si-alloy based material for engine applications*, Journal of Materials Engineering and Performance, 12, pp. 288-297.
12. Nowak, M., Hari-Babu, N., 2011, *Novel grain refiner for hypo and hyper-eutectic Al-Si alloys*, LMT 2011 Conf paper, Materials Science Form, 690, pp. 49-52.
13. Flemings, M.C., 1974, *Solidification processing*, Metallurgical and Materials Transactions, 5, pp. 2121-2134.
14. Abboud, J., Mazumder, J., 2020, *Developing of nano sized fibrous eutectic silicon in hypereutectic Al–Si alloy by laser remelting*, Scientific Reports, 10, pp. 1-18.
15. McDonald, S. D., Nogita, K., Dahle, A. K., 2004, *Eutectic nucleation in Al-Si alloys*, Acta Materialia, 52, pp. 4273-4280.
16. Chou, R., Milligan, J., Paliwal, M., Brochu, M., 2015, *Additive manufacturing of Al-12Si alloy via pulsed selective laser melting*, JOM: the journal of the Minerals, Metals & Materials Society, 67, pp. 590-596.
17. Siddique, S., Imran, M., Wycisk, E., Emmelmann, C., Walther, F., 2015, *Influence of process-induced microstructure and imperfections on mechanical properties of AlSi12 processed by selective laser melting*, Journal of Materials Processing Technology, 221, pp. 205-213.

18. Kim, D.-K., Hwang, J.-H., Kim, E.-Y., Heo, Y.-U., Woo, W., Choi, S.-H., 2017, *Evaluation of the stress-strain relationship of constituent phases in AlSi10Mg alloy produced by selective laser melting using crystal plasticity FEM*, Journal of Alloys and Compounds, 714, pp. 687-697.

19. Silva, A. D., Wang, S., Volpp, J., Kaplan, A.F.H., 2020, *Vertical laser metal wire deposition of Al-Si alloys*, Procedia CIRP, 94, pp. 341-345.

20. Huang, W., Chen, S., Xiao, J., Jiang, X., Jia, Y., 2021, *Laser wire-feed metal additive manufacturing of the Al alloy*, Optics & Laser Technology, 134, 106627.

21. Kolubaev, E., Rubtsov, V., Chumaevskii, A., Astafurova, E., 2022, *Micro-, meso- and macrostructural design of bulk metallic and polymetallic materials by wire-feed electron-beam additive manufacturing*, Physical Mesomechanics, 25, pp. 479-491.

22. Osipovich, K., Kalashnikov, K., Chumaevskii, A., Gurianov, D., Kalashnikova, T., Vorontsov, A., Zykova, A., Utyaganova, V., Panfilov, A., Nikolaeva, A., Dobrovolskii, A., Rubtsov, V., Kolubaev, E., 2023, *Wire-feed electron beam additive manufacturing: A review*, Metals, 13, 279.

23. Zhu, Z., Hu, Z., Seet, H.L., Liu, T., Liao, W., Ramamurty, U., Nai, S.M.L., 2023, *Recent progress on the additive manufacturing of aluminum alloys and aluminum matrix composites: Microstructure, properties, and applications*, International Journal of Machine Tools and Manufacture, 190,104047.

24. Balokhonov, R., Zemlianov, A., Utyaganova, V., Gatiyatullina, D., Romanova, V., 2023, *Two-scale computational analysis of deformation and fracture in an Al-Si composite material fabricated by electron beam wire-feed additive manufacturing*, Metals, 13, 1465.

25. Zemlyanov, A.V., Gatiyatullina, D.D., Utyaganova, V.R., Dymnich, E., Shamarin, N.N., Nikonov, S.Y., Romanova, V.A., Kulkov, A.S., Balokhonov, R.R., 2023, *A study of deformation and fracture of the eutectic in an additively manufactured Al-Si composite alloy*, Physical Mesomechanics, 26, pp. 678-690.

26. Wang, B.B., Xie, G.M., Wu, L.H., Xue, P., Ni, D.R., Xiao, B.L., Liu, Y.D., Ma, Z.Y., 2021, *Grain size effect on tensile deformation behaviors of pure aluminum*, Materials Science and Engineering: A, 820, 141504.

27. Wejrzanowski, T., Lewandowska, M., Kurzydłowski, K. J., 2010, *Stereology of nano-materials*, Image Analysis and Stereology, 29(1), pp. 1-12.